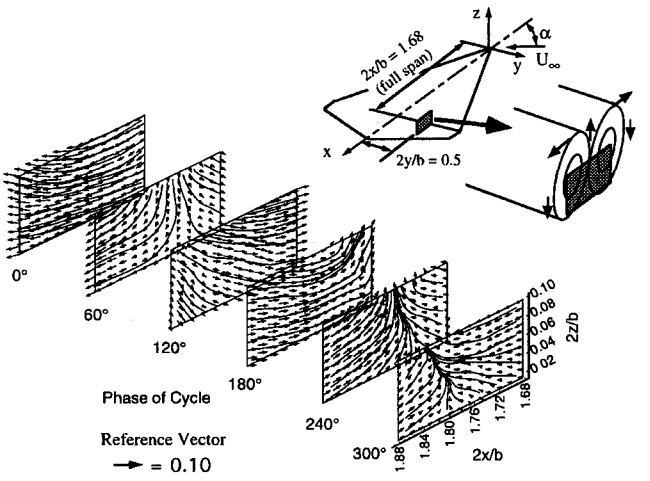

Fig. 3 Vectors of fluctuating velocity, measured using laser velocimetry, of ensemble-averaged in several discrete 12-deg phase intervals of a trigger signal at the dominant fluctuation frequency generated from a surface hot-film sensor at $2x/b = 1.68$.

structures convect downstream with respect to time (phase). Single-point measurements above the core were 180 deg out of phase with corresponding points below, suggesting a helical geometry of propagation of the disturbance. The structure scale is on the order of the vortex radius; the convection speed based on this length scale and the cycle period is $0.15U_\infty$.

The formation of a rotating structure in an environment with mean streamline curvature is analogous to Taylor–Görtler type vortices[8,9] and indicates the interaction between the centrifugal forces and the radial pressure gradient of the primary vortex near the surface. This type of instability is based on Rayleigh's second theorem on the stability of a velocity profile; the conditions exist in the surface shear layer under a postburst vortex, whose tangential velocity profile resembles that of solid-body rotation. Ludwieg[10] proposed that this type of three-dimensional disturbance causes the breakdown of free vortices over delta wings. Disturbances of this nature could explain the focusing and amplification mechanisms away from the core.

Some similarities are observed with Gursul's helical mode explanation.[7] The trajectory of the structures does appear to be helical, as may be expected given the mean streamlines of the vortex flow. In addition, the spectral frequency remains approximately constant over a crossflow plane at a given chordwise location. However, several features do not fit the helical mode theory. The orientation of the structures, with velocity components measured unambiguously, is essentially spanwise, not chordwise as postulated by Gursul based on hot-film data. The phenomenon clearly does not originate in the core region, postburst or otherwise. It originates in the shear layer near the surface.

Conclusions

Velocity fluctuations occurring in the postburst flowfield over a 59.3-deg delta wing were studied using laser sheet videography, hot-film anemometry, and LV.

1) Viewed in a plane parallel to the wing surface, surface layer streaklines oscillated at a frequency that matched that of the spectral peak measured using hot-film anemometry.

2) Viewed in a vertical plane along a ray inboard of the secondary separation line, the streaklines rolled up and erupted off the surface, indicating counter-rotating structures.

3) Spectra measured using LV above the surface matched those measured by a surface hot film.

4) Velocity measurements, triggered from the surface hot-film signal, resolved into the phase of the spectral peak frequency and ensemble averaged, showed organized, counter-rotating structures in two vertical planes aligned with rays. These clearly indicate vortical structures whose axes are oriented approximately spanwise, convecting at a speed of roughly $0.15U_\infty$.

5) The nature of the structure appears consistent with a centrifugal instability arising between the primary vortex and the surface.

Acknowledgments

This work was performed under a U.S. Air Force Office of Scientific Research grant monitored by Dan Fant and Len Sakell. Special thanks are given to the Experimental Aerodynamics Group for its assistance.

References

[1]Colvin, B. J., Mullans, R. E., Paul, R. J., and Roos, H. N., "F-15 Vertical Tail Vibration Investigations," McDonnell–Douglas Corp., Rept. A6114, St. Louis, MO, Sept. 1979.

[2]Komerath, N. M., Schwartz, R. J., and Kim, J. M., "Flow over a Twin-Tailed Aircraft at Angle-of-Attack, Part II: Temporal Characteristics," *Journal of Aircraft*, Vol. 29, No. 4, 1992, pp. 553–558.

[3]Klein, M. A., Hubner, J. P., and Komerath, N. M., "Spectral Measurements in Vortex Flow over Swept-Winged Configurations at High Angle of Attack," AIAA Paper 94-1804, June 1994.

[4]Hubner, J. P., and Komerath, N. M., "Trajectory Mapping of Quasi-Periodic Structures in a Vortex Flow," *Journal of Aircraft*, Vol. 32, No. 3, 1995, pp. 493–500.

[5]Hubner, J. P., and Komerath, N. M., "Visualization of Quasiperiodic Structures in a Vortex Flow," AIAA Paper 94-0624, Jan. 1994.

[6]Redionitis, O. K., Stapountzis, H., and Telionis, D. P., "Vortex Shedding over Delta Wings," *AIAA Journal*, Vol. 28, No. 5, 1990, pp. 944–946.

[7]Gursul, I., "Unsteady Flow Phenomena over Delta Wings at High Angle of Attack," *AIAA Journal*, Vol. 32, No. 2, 1994, pp. 225–231.

[8]Schlichting, H., *Boundary Layer Theory*, 7th ed., McGraw–Hill, New York, 1979, pp. 525–535.

[9]Saric, W., "Görtler Vortices," *Annual Review of Fluid Mechanics*, Vol. 26, 1994, pp. 379–409.

[10]Ludwieg, H., "An Explanation of the Instability of the Free Vortex Cores Occurring over Delta Wings with Raised Edges," NASA TM-75861, 1980; translated from *Zeitschrift für Flugwissenschaften*, Vol. 10, No. 6, 1962, pp. 242–249.

Three-Dimensional Analysis of Simply Supported Laminated Cylindrical Shells with Arbitrary Thickness

Jianping Zhou* and Bingen Yang†
University of Southern California, Los Angeles, California 90089-1453

Introduction

MODELING of composite cylindrical shells and panels is usually based on one of the following three types of theories: the classic laminated theory (CLT), the shear deformation theories, and the three-dimensional elasticity theory. Because of the high ratio of in-plane Young's modulus to transverse shear modulus, ignorance of the shell transverse shear deformation in CLT can lead to serious errors even for thin cylindrical shells/panels. Although the shear deformation theories have met with success in many cases, three-dimensional elasticity solutions are still needed for the purpose of assessment of various approximate theories and better understanding of actual distributions of stresses, strains, and displacements in composite shells, especially for thick shells.[1,3,4,6,7] This Note presents an innovative method for analysis of simply supported (SS), multilayered, orthotropic, circular cylindrical shells and panels with arbitrary shell thickness. In this method, the three-dimensional displacements and stresses of laminated shells are determined by a

Received Sept. 13, 1994; revision received Oct. 13, 1995; accepted for publication Nov. 1, 1995.

*Visiting Scholar, Department of Mechanical Engineering; currently Professor, Department of Astronautics, National University of Defence Technology, Changsha, Hunan 410073, People's Republic of China.

†Associate Professor, Department of Mechanical Engineering. Member AIAA.

lamina synthesis procedure that is based on Fourier expansion and a spatial state-space formulation. The high accuracy and efficiency of the proposed method is shown in numerical examples.

Approach

A composite circular cylindrical shell of NL layers is shown in Fig. 1, where L, H, and R are the length, thickness, and midsurface radius of the shell, respectively; r_k and h_k are the midsurface radius and thickness of the kth layer, respectively; and x, r, and θ are the coordinates in the longitudinal, radial, and circumferential directions, respectively. The shell is SS at its two ends and is under arbitrary static loads. Shown in the figure is a patch load applied on the outer surface, where L_p is the width of load distribution in the x direction and θ_p is the subtended angle of the load in the θ direction. Assume that the shell is orthotropically laminated; namely, the reinforcing fibers of each layer are aligned with either x or θ direction. An SS laminated circular cylindrical panel of a subtended angle $2\theta_0$ can be similarly described.

Let $u^{(k)}$, $v^{(k)}$, and $w^{(k)}$ be the displacements of the kth layer in the x, θ, and r directions, respectively. Let $\sigma_r^{(k)}, \ldots, \tau_{x\theta}^{(k)}$ be the stresses of the layer. Assume the layer is of orthotropic material with elastic coefficients $C_{ij}^{(k)}$ and under body forces f_x, f_θ, and f_z. The cylindrical shell/panel satisfies the SS boundary conditions at $x = 0$ and L:

$$\sigma_x^{(k)} = v^{(k)} = w^{(k)} = 0 \tag{1a}$$

The panel also satisfies the conditions at its two other edges at $\theta = \pm\theta_0$:

$$\sigma_\theta^{(k)} = u^{(k)} = w^{(k)} = 0 \tag{1b}$$

On the outer surface of the shell ($r = h_{NL}/2$)

$$\sigma_r^{(NL)} = \breve{\sigma}_r(x,\theta), \quad \tau_{\theta r}^{(NL)} = \breve{\tau}_{\theta r}(x,\theta), \quad \tau_{xr}^{(NL)} = \breve{\tau}_{xr}(x,\theta) \tag{1c}$$

and on the inner surface ($r = -h_1/2$)

$$\sigma_r^{(1)} = \hat{\sigma}_r(x,\theta), \quad \tau_{\theta r}^{(1)} = \hat{\tau}_{\theta r}(x,\theta), \quad \tau_{xr}^{(1)} = \hat{\tau}_{xr}(x,\theta) \tag{1d}$$

where $\breve{\sigma}_r(x,\theta), \ldots, \hat{\tau}_{xr}(x,\theta)$ are given surface loads. Also, the displacements and stresses of a laminated shell/panel should be continuous at the interface between any two adjacent layers; namely, for $k = 1, 2, \ldots, NL - 1$,

$$\begin{aligned} u^{(k)}(x,\theta,h_k/2) &= u^{(k+1)}(x,\theta,-h_{k+1}/2) \\ \sigma_r^{(k)}(x,\theta,h_k/2) &= \sigma_r^{(k+1)}(x,\theta,-h_{k+1}/2)\ldots \end{aligned} \tag{2}$$

The proposed solution procedure takes three steps: 1) expand the displacements of each lamina in Fourier series in θ and x reducing the governing elasticity equations to a sequence of decoupled equations in z; 2) transform the resulting equations into a state-space form; and 3) assemble the composite shell or panel from the laminas by imposing the continuity conditions (2).

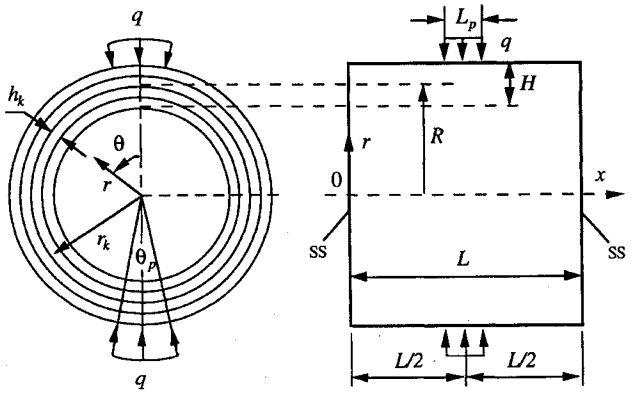

Fig. 1 Laminated circular cylindrical shell.

The unknown displacements and given loads are expanded into the Fourier series.

Displacements:

$$\begin{aligned} u^{(k)}(x,\theta,z) &= \sum_{m=1}^{\infty}\sum_{n=0}^{\infty} U_k^{(mn)}(z)\cos\alpha_m x\cos\beta_n\theta \\ v^{(k)}(x,\theta,z) &= \sum_{m=1}^{\infty}\sum_{n=1}^{\infty} V_k^{(m)}(z)\sin\alpha_m x\sin\beta_n\theta \\ w^{(k)}(x,\theta,z) &= \sum_{m=1}^{\infty}\sum_{n=0}^{\infty} W_k^{(mn)}(z)\sin\alpha_m x\cos\beta_n\theta \end{aligned} \tag{3a}$$

Body forces:

$$\begin{aligned} f_x(x,\theta,z) &= \sum_{m=1}^{\infty}\sum_{n=0}^{\infty} f_x^{(mn)}(z)\cos\alpha_m x\cos\beta_n\theta \\ f_\theta(x,\theta,z) &= \sum_{m=1}^{\infty}\sum_{n=1}^{\infty} f_\theta^{(mn)}(z)\sin\alpha_m x\sin\beta_n\theta \\ f_r(x,\theta,z) &= \sum_{m=1}^{\infty}\sum_{n=0}^{\infty} f_r^{(mn)}(z)\sin\alpha_m x\cos\beta_n\theta \end{aligned} \tag{3b}$$

Surface loads:

$$\begin{aligned} \breve{\sigma}_r(x,\theta) &= \sum_{m=1}^{\infty}\sum_{n=0}^{\infty} \breve{\sigma}_r^{(mn)}\sin\alpha_m x\cos\beta_n\theta \\ \breve{\tau}_{\theta r}(x,\theta) &= \sum_{m=1}^{\infty}\sum_{n=1}^{\infty} \breve{\tau}_{\theta r}^{(mn)}\sin\alpha_m x\sin\beta_n\theta \\ \breve{\tau}_{xr}(x,\theta) &= \sum_{m=1}^{\infty}\sum_{n=1}^{\infty} \breve{\tau}_{xr}^{(mn)}\cos\alpha_m x\cos\beta_n\theta \\ \hat{\sigma}_r(x,\theta) &= \sum_{m=1}^{\infty}\sum_{n=0}^{\infty} \hat{\sigma}_r^{(mn)}\sin\alpha_m x\cos\beta_n\theta \\ \hat{\tau}_{\theta r}(x,\theta) &= \sum_{m=1}^{\infty}\sum_{n=1}^{\infty} \hat{\tau}_{\theta r}^{(mn)}\sin\alpha_m x\sin\beta_n\theta \\ \hat{\tau}_{xr}(x,\theta) &= \sum_{m=1}^{\infty}\sum_{n=1}^{\infty} \hat{\tau}_{xr}^{(mn)}\cos\alpha_m x\cos\beta_n\theta \end{aligned} \tag{3c}$$

Here $\alpha_m = m\pi/L$, $\beta_n = n$ for a cylindrical shell, and $\beta_n = (n - \frac{1}{2})\pi/\theta_0$ for a cylindrical panel.

Define a dimensionless coordinate ξ and a parameter ρ_k by

$$r = r_k(1 + \rho_k\xi), \qquad \rho_k = \tfrac{1}{2}(h_k/r_k), \qquad \xi = (2z/h_k) \in [-1, 1] \tag{4}$$

By the linear elasticity theory,[5] the equations governing the unknown displacement functions in Eq. (3a) are derived as

$$\begin{aligned} (1+\rho_k\xi)^2 U_k''(z) &= \left(a_{21} + 2\rho_k\xi b_{21} + \rho_k^2\xi^2 b_{21}\right)U_k(z) \\ &\quad + a_{22}(1+\rho_k\xi)U_k'(z) + a_{23}(1+\rho_k\xi)V_k(z) \\ &\quad + a_{25}(1+\rho_k\xi)W_k(z) + a_{26}(1+\rho_k\xi)^2 W_k'(z) + \bar{f}_x^{(k)}(z) \\ (1+\rho_k\xi)^2 V_k''(z) &= a_{41}(1+\rho_k\xi)U_k(z) \\ &\quad + \left(a_{43} + 2\rho_k\xi b_{43} + \rho_k^2\xi^2 b_{43}\right)V_k(z) + a_{22}(1+\rho_k\xi)V_k'(z) \\ &\quad + a_{45}W_k(z) + a_{46}(1+\rho_k\xi)W_k'(z) + \bar{f}_\theta^{(k)}(z) \\ (1+\rho_k\xi)^2 W_k''(z) &= a_{61}(1+\rho_k\xi)U_k(z) \\ &\quad + a_{62}(1+\rho_k\xi)^2 U_k'(z) + a_{63}V_k + a_{64}(1+\rho_k\xi)V_k' \\ &\quad + \left(a_{65} + 2\rho_k\xi b_{65} + \rho_k^2\xi^2 b_{65}\right)W_k(z) \\ &\quad + a_{22}(1+\rho_k\xi)W_k'(z) + \bar{f}_r^{(k)}(z) \end{aligned} \tag{5}$$

where for simplicity the superscript (mn) has been dropped and the prime denotes d/dz. The constants a_{ij} and b_{ij} are given in terms of α_m, β_n, r_k, and $C_{ij}^{(k)}$; and $\bar{f}_x^{(k)}(z)$, $\bar{f}_\theta^{(k)}(z)$, and $\bar{f}_r^{(k)}(z)$ are the body forces multiplied by some constants.

In many practical situations, each lamina is thin enough that, according to Eq. (4), $\rho_k \ll 1$. If it is not so, we can divide the lamina into a number of sublayers so that $\rho_k \ll 1$ for the sublayers. Either way, it is appropriate to assume that $1 + \rho_k \xi \approx 1$. Under the assumption, Eqs. (5), which become ordinary differential equations with constant coefficients, are cast in the state-space form,

$$\frac{\mathrm{d}\eta_0^{(k)}}{\mathrm{d}z} = F^{(k)}\eta_0^{(k)} + \bar{f}^{(k)}, \qquad z \in \left[-\frac{h_k}{2}, \frac{h_k}{2}\right] \tag{6}$$

where $\eta_0^{(k)} = \{U_k \;\; U_k' \;\; V_k \;\; V_k' \;\; W_k \;\; W_k'\}^T$, $\bar{f}^{(k)} = \{0 \;\; \bar{f}_x^{(k)} \;\; 0 \;\; \bar{f}_\theta^{(k)} \;\; 0 \;\; \bar{f}_r^{(k)}\}^T$, and the six-by-six matrix $F^{(k)}$ is composed of constants a_{ij}. Substitute Eq. (3a) into the strain-displacement and constitutive relations[5] to obtain the strain and stress components of the kth layer

$$\begin{Bmatrix} \varepsilon_x^{(k)} \\ \vdots \\ \gamma_{x\theta}^{(k)} \end{Bmatrix} = \begin{Bmatrix} \hat{\varepsilon}_x^{(k)} \sin\alpha_m x \cos\beta_n\theta \\ \vdots \\ \hat{\gamma}_{x\theta}^{(k)} \cos\alpha_m x \sin\beta_n\theta \end{Bmatrix} \tag{7a}$$

$$\begin{Bmatrix} \sigma_x^{(k)} \\ \vdots \\ \tau_{x\theta}^{(k)} \end{Bmatrix} = \begin{Bmatrix} \hat{\sigma}_x^{(k)} \sin\alpha_m x \cos\beta_n\theta \\ \vdots \\ \hat{\tau}_{x\theta}^{(k)} \cos\alpha_m x \sin\beta_n\theta \end{Bmatrix} \tag{7b}$$

where $\hat{\varepsilon}_{ij}^{(k)}(z)$ and $\hat{\sigma}_{ij}^{(k)}(z)$ are expressed in terms in $\eta_0^{(k)}$

$$\left\{\hat{\varepsilon}^{(k)}\right\} = [B(r)]\eta_0^{(k)}, \qquad \left\{\hat{\sigma}^{(k)}\right\} = \left[\bar{C}^{(k)}\right]\eta_0^{(k)}$$
$$\left[\bar{C}^{(k)}\right] = \left[C^{(k)}\right][B(r)] \tag{8}$$

where $\{\hat{\varepsilon}^{(k)}\} = \left\{\hat{\varepsilon}_x^{(k)} \;\; \hat{\varepsilon}_\theta^{(k)} \;\; \hat{\varepsilon}_r^{(k)} \;\; \hat{\gamma}_{\theta r}^{(k)} \;\; \hat{\gamma}_{xr}^{(k)} \;\; \hat{\gamma}_{x\theta}^{(k)}\right\}^T$; $\{\hat{\sigma}^{(k)}\} = \{\hat{\sigma}_x^{(k)} \;\; \hat{\sigma}_\theta^{(k)} \;\; \hat{\sigma}_r^{(k)} \;\; \hat{\tau}_{\theta r}^{(k)} \;\; \hat{\tau}_{xr}^{(k)} \;\; \hat{\tau}_{x\theta}^{(k)}\}^T$; $[B(r)]$ consists of the elements $\pm\beta_n/r$, $\pm 1/r$, $\pm\alpha_m$, 1, and 0; and the constitutive matrix $[C^{(k)}]$ contains the elastic coefficients $C_{ij}^{(k)}$. By Eqs. (7) and (8), the boundary conditions (1) are cast in

$$M^{(1)}\eta_0^{(1)}(-h_1/2) + N^{NL}\eta_0^{(NL)}(h_{NL}/2) = \gamma_0 \tag{9}$$

where $\gamma_0 = \{\breve{\sigma}_z \;\; \breve{\tau}_{\theta z} \;\; \hat{\tau}_{xz} \;\; \breve{\sigma}_z \;\; \breve{\tau}_{\theta z} \;\; \breve{\tau}_{xz}\}^T$, and $M^{(1)}$ and $N^{(NL)}$ are composed of the elements of $[\bar{C}^{(1)}]$ and $[\bar{C}^{(NL)}]$, respectively. The solution to the state-space equation (6) is of the form

$$\eta_0^{(k)}(z) = e^{F^{(k)}z}\left(\int_{-h_k/2}^{z} e^{-F^{(k)}\tau}\bar{f}^{(k)}\,\mathrm{d}\tau + \bar{\eta}_0^{(k)}\right) \tag{10}$$

where $\bar{\eta}_0^{(k)}$ is a constant vector to be determined.

The vectors $\eta_0^{(k)}$, $k = 1, 2, \ldots, NL$, are coupled by the layer interface and have to be determined through synthesis of all of the laminas by imposing the continuity conditions (2) and the boundary conditions (9). Two synthesis techniques for determining $\bar{\eta}_0^{(k)}$ are proposed: the connection matrix method and the nodal displacement method.

Connection Matrix Method

The continuity conditions (2) are rewritten in the matrix form

$$L_k\eta_0^{(k)}(h_k/2) = L_{k+1}\eta_0^{(k+1)}(-h_{k+1}/2) \tag{11}$$

where L_k consists of the elements of $[\bar{C}^{(k)}]$. Substituting Eq. (11) into Eq. (10) gives

$$\bar{\eta}_0^{(k+1)} = e^{0.5h_{k+1}F^{(k+1)}}L_{k+1}^{-1}L_k e^{0.5h_kF^{(k)}}\left[\hat{f}^{(k)} + \bar{\eta}_0^{(k)}\right] \tag{12}$$

where

$$\hat{f}^{(k)} = \int_{-0.5h_k}^{0.5h_k} e^{-F^{(k)}\tau}\bar{f}^{(k)}(\tau)\,\mathrm{d}\tau$$

Apply the preceding recurrently to find

$$\bar{\eta}_0^{(k)} = \sum_{i=2}^{k} Q_i^{(k)}\bar{f}^{(i-1)} + Q_2^{(k)}\bar{\eta}_0^{(1)}, \qquad k = 2, 3, \ldots, NL \tag{13}$$

where

$$\bar{\eta}_0^{(1)} = \left[M^{(1)}e^{-0.5h_1F^{(1)}} + N^{(NL)}e^{0.5h_{NL}F^{(NL)}}Q_2^{(NL)}\right]^{-1}$$
$$\times\left[\gamma_0 - N^{(NL)}e^{0.5h_{NL}F^{(NL)}}\sum_{k=1}^{NL}Q_{k+1}^{(NL)}\bar{f}^{(k)}\right]$$

and

$$Q_k^{(m)} = \Pi_{i=k}^{m}e^{-0.5h_iF^{(i)}}L_i^{-1}L_{i-1}e^{0.5h_{i-1}F^{(i-1)}}$$

Nodal Displacement Method

Define the nodes of the shell as the inner and outer surfaces of the shell and the interior interfaces on the layers. The nodal displacements are in the vector form

$$u_0 = \{U_1(-h_1/2) \quad V_1(-h_1/2) \quad W_1(-h_1/2)\}^T$$
$$u_k = \{U_k(h_k/2) \quad V_k(h_k/2) \quad W_k(h_k/2)\}^T, \qquad k = 1, 2, \ldots, NL$$

It is from Eqs. (10) and (2) that

$$\bar{\eta}_0^{(k)} = H_k\left(\begin{Bmatrix} u_{k-1} \\ u_k \end{Bmatrix} - \begin{Bmatrix} 0_{3\times 1} \\ I_q\bar{f}^{(k)} \end{Bmatrix}\right) \tag{14}$$

where

$$\bar{f}^{(k)} = e^{0.5h_kF^{(k)}}\int_{-0.5h_k}^{0.5h_k} e^{-F^{(k)}\tau}\bar{f}^{(k)}(\tau)\,\mathrm{d}\tau$$

and H_k and I_q are constant matrices. Substituting Eq. (14) into the stress continuity conditions (2) for all of the interfacing nodes and imposing force balance at the inner and outer surfaces yield

$$[K]\{u\} = \{Q\} \tag{15}$$

where $\{u\} = \{u_0^T u_1^T u_2^T \cdots u_{NL}^T\}^T$, $\{Q\}$ is the global load vector constructed from $\bar{f}^{(k)}$, and $[K]$ the stiffness matrix assembled from H_k and $[\bar{C}^{(k)}]$ of all of the layers. Solving Eq. (15) for the nodal displacements and substituting the result into Eq. (14) gives $\bar{\eta}_0^{(k)}$.

Once $\bar{\eta}_0^{(k)}$ is determined, either by Eq. (13) or Eq. (15), the displacement and stress distributions of each layer can be estimated by substituting Eq. (10) into Eqs. (3a) and (7b).

Numerical Results

In the numerical simulation, it is assumed that the shell radius-to-length ratio $R/L = 1$ with $L = 10$. All laminas have the same material properties: $E_L/E_T = 11.53$, $G_{LT}/E_T = 0.56$, $G_{TT}/E_T = 0.379$, $\nu_{LT} = 0.3$, and $\nu_{TT} = 0.32$. Here the subscripts L and T represent the longitudinal and transverse directions of the fibers in a lamina.

Single-layered shells are first analyzed to validate the proposed method. Let the fibers of the shell layer be along the longitudinal (x) direction. The shell is under a sinusoidal load on its outer surface: $\breve{\sigma}_r = q\sin(\pi x/L)\cos\theta$, $\breve{\tau}_{\theta r} = \breve{\tau}_{xr} = \hat{\sigma}_r = \hat{\tau}_{\theta r} = \hat{\tau}_{xr} = 0$. To

Table 1 Displacement and stresses of a single-layered cylindrical shell ($R/H = 2$, $x = L/2$, and $\theta = 0$)

NL	$\bar{w}\|_{\text{mid}}$	$\bar{\sigma}_x\|_{\text{outer}}$	$\bar{\sigma}_x\|_{\text{inner}}$	$\bar{\sigma}_\theta\|_{\text{outer}}$	$\bar{\sigma}_\theta\|_{\text{inner}}$
1	−5.7249	−1.0898	0.8755	−0.2154	−0.0665
2	−5.6998	−1.0930	0.8729	−0.2198	−0.0651
4	−5.6981	−1.0951	0.8734	−0.2200	−0.0647
8	−5.6980	−1.0957	0.8735	−0.2202	−0.0647
16	−5.6980	−1.0958	0.8734	−0.2203	−0.0647

Table 2 Displacement and stresses of a single-layered cylindrical shell ($x = L/2$ and $\theta = 0$)

	R/H	Proposed	Ref. 3	CLT	HSDT
$\bar{w}\|_{\text{mid}}$	2	−5.6980	−5.711	−1.0027	−5.0466
	5	−1.4339	−1.436	−0.8502	−1.3506
	10	−0.6283	−0.629	−0.5513	−0.6077
	20	−0.2360	−0.236	−0.2292	−0.2319
	100	−0.01168	−0.012	−0.01163	−0.01163
$\bar{\sigma}_x\|_{\text{outer}}$	2	−1.0957	−1.101	−0.5784	−0.8629
	5	−0.5097	−0.510	−0.4924	−0.4757
	10	−0.3098	−0.310	−0.3217	−0.2993
	20	−0.1329	−0.133	−0.1357	−0.1305
	100	−0.00769	−0.0077	−0.00769	−0.00765
$\bar{\sigma}_x\|_{\text{inner}}$	2	−0.8735	−0.873	−0.5740	−0.9249
	5	−0.5230	−0.523	−0.4848	−0.4919
	10	−0.3105	−0.311	−0.3121	−0.2983
	20	−0.1247	−0.127	−0.1278	−0.1246
	100	−0.00571	−0.0057	−0.00568	−0.00567
$\bar{\sigma}_\theta\|_{\text{outer}}$	2	−0.2202	−0.218	−0.0352	−0.1019
	5	−0.0853	−0.085	−0.0521	−0.0689
	10	−0.0634	−0.063	−0.0573	−0.0592
	20	−0.0439	−0.044	−0.0433	−0.0427
	100	−0.01011	−0.0101	−0.01011	−0.01006
$\bar{\sigma}_\theta\|_{\text{inner}}$	2	−0.0647	−0.065	−0.0029	−0.0648
	5	−0.0469	−0.047	−0.0195	−0.0447
	10	−0.0455	−0.045	−0.0362	−0.0438
	20	−0.0369	−0.037	−0.0345	−0.0361
	100	−0.00976	−0.0097	−0.00966	−0.00971

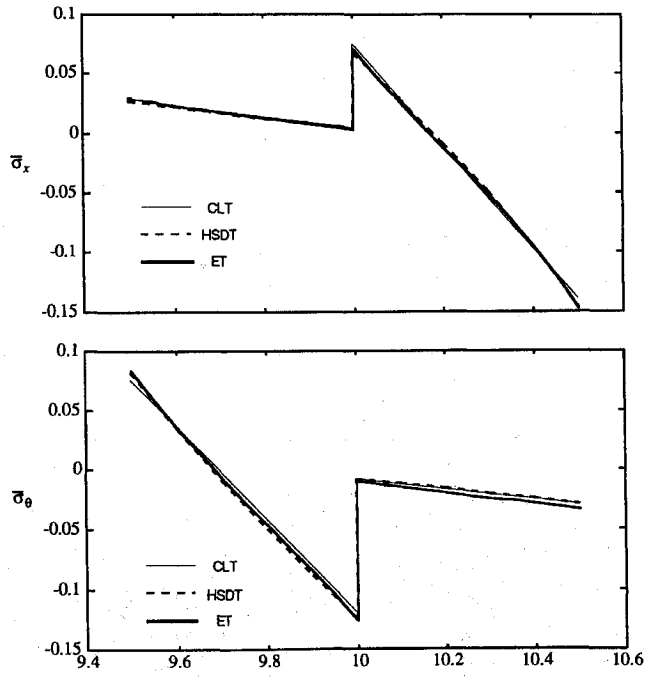

Fig. 2 Stress distributions of a two-layered shell along the radial direction: $R/H = 10$, $NL = 2$, and 90/0; $x = L/2$ and $\theta = 0$.

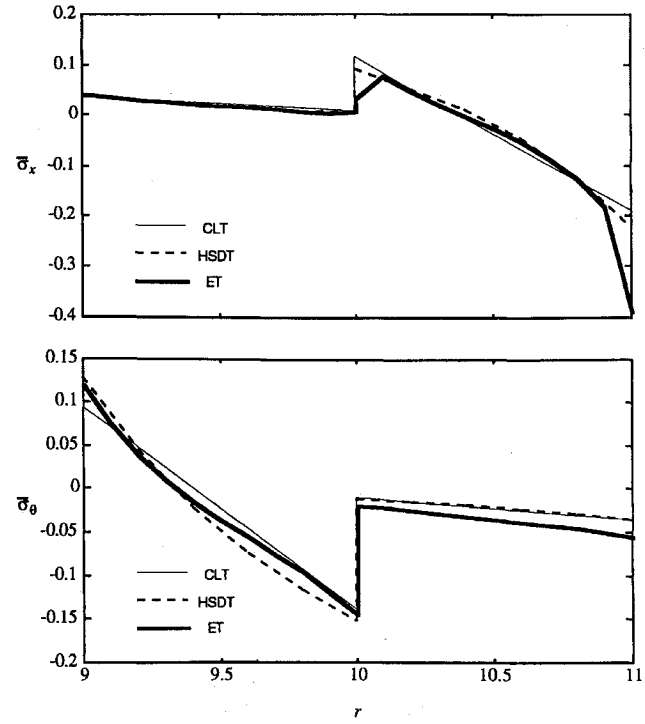

Fig. 3 Stress distributions of a two-layered shell along the radial direction: $R/H = 5$, $NL = 2$, and 90/0; $x = L/2$ and $\theta = 0$.

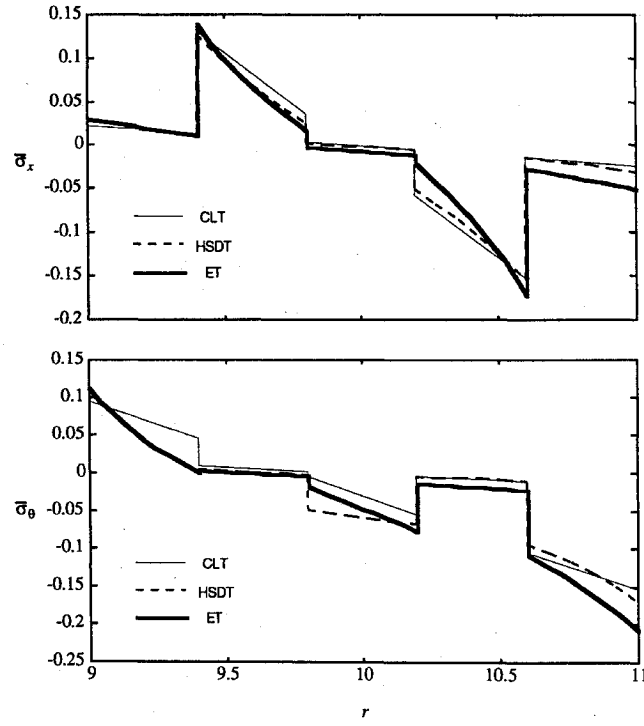

Fig. 4 Stress distributions of a five-layered shell along the radial direction: $R/H = 5$, $NL = 5$, and 90/0/90/0/90; $x = L/2$ and $\theta = 0$.

increase accuracy, the single-layered shell is virtually divided into NL virtual layers of equal thickness. Shown in Table 1 are the nondimensional displacement and stresses of a thick shell ($R/H = 2$) at $x = L/2$ and $\theta = 0$. Here $\bar{w} = w \times 100E_T H^3/(qR^4)$; $(\bar{\sigma}_x, \bar{\sigma}_\theta) = (\sigma_x, \sigma_\theta) \times H^2/R^2$; $\bar{w}|_{\text{mid}}$ is the displacement $\bar{w}$ at the shell midsurface; and $\bar{\sigma}_x|_{\text{outer}}$, $\bar{\sigma}_x|_{\text{inner}}$, $\bar{\sigma}_\theta|_{\text{outer}}$, and $\bar{\sigma}_\theta|_{\text{inner}}$ are the stresses $\bar{\sigma}_x$ and $\bar{\sigma}_\theta$ at the outer and inner surfaces of the shell, respectively. The convergence of the proposed method is excellent: two virtual layers ($NL = 2$) are adequate to yield the accurate predictions, with relative errors less than 0.5%.

In Table 2, the proposed method is compared with the CLT, the high-order shear deformation theory (HSDT),[2] and the three dimensional elasticity solution given in Ref. 3, for $R/H = 2, 5, 10, 20,$ and 100. It is seen that CLT is reasonably accurate only when $R/H \geq 20$, whereas HSDT is good for $R/H \geq 10$. The proposed method is valid for all of the R/H values and gives predictions that are in agreement with those of Ref. 3.

As a second example, cross-ply, orthotropically laminated cylindrical shells are modeled. The thickness of every layer is the same: $h_k = H/NL$. The laminating sequence, which starts with the first (inner) layer, is 90/0/90..., where 90 deg means that the fibers are aligned with the θ direction and 0 deg the x direction. The shell is subject to the patch load shown in Fig. 1. The width and subtended angle of the load are taken as $L_p = L/4$ and $\theta_p = \pi/8$.

The proposed three-dimensional elasticity theory is compared with the CLT and the HSDT. Figure 2 shows the distributions of the stresses $\bar{\sigma}_x$ and $\bar{\sigma}_\theta$ of a two-layered shell along the radial direction. Because the shell is thin ($R/H = 10$), the predictions by these theories have small deviations. However, when the shell is relatively thick, say $R/H = 5$, CLT and HSDT lead to large errors, as shown in Figs. 3 and 4 where the stress distributions of a two-layered shell and a five-layered shell are plotted. Apparently, in this case, three-dimensional elasticity theories have to be utilized.

Concluding Remarks

The proposed method is highly accurate in predicting the three-dimensional stresses and displacements of composite shells with arbitrary thickness. One advantage of the method is that various loads and lamina properties are systematically treated by the explicit and compact matrix form of the spatial state-space formulation, which is convenient for computing coding.

For an orthotropic cylindrical shell, the transverse deformation and three-dimensional deformation effects are significant even if the shell is moderately thick. With $L/R = 1$, the classic laminated theory can only be used with reasonable accuracy for $R/H \geq 20$ and higher order shear deformation theory is reliable for $R/H \geq 10$. It is seen that three-dimensional elastic deformation must be taken into consideration even for moderately thick shells, not to mention very thick shells. The proposed method is valid for both thin and thick shells with arbitrary R/H values.

Although this work has focused on SS shells, the proposed method is readily extended to more general boundary conditions. Also, the method can be applied to dynamic problems of laminated shells when combined with the distributed transfer function method.[8]

Acknowledgment

This work was partially supported by the U.S. Army Research Office.

References

[1]Bhaskar, K., and Varadan, T. K., "Benchmark Elasticity Solution for Locally Loaded Laminated Orthotropic Cylindrical Shells," *AIAA Journal*, Vol. 32, No. 3, 1994, pp. 627–632.

[2]Bhimaraddi, A., and Stevens, L. K., "On the Higher Order Theories in the Plates and Shells," *International Journal of Structures*, Vol. 6, No. 1, 1986, pp. 35–50.

[3]Chandrashekhara, K., and Kumar, B. S., "Static Analysis of Thick Laminated Circular Cylindrical Shells," *Journal of Pressure Vessel Technology*, Vol. 115, May 1993, pp. 193–200.

[4]Flugge, W., and Kelkar, V. S., "The Problem of an Elastic Circular Cylinder," *International Journal of Solids and Structures*, Vol. 4, 1968, pp. 397–420.

[5]Fung, Y. C., *Foundations of Solid Mechanics*, Prentice–Hall, Englewood Cliffs, NJ, 1968.

[6]Misovec, A. P., and Kempner, J., "Approximate Elasticity Solution for Orthotropic Cylinder Under Hydrostatic Pressure and Band Load," *Journal of Applied Mechanics*, Vol. 37, No. 1, 1970, pp. 101–108.

[7]Ren. J. G., "Analysis of Simply-Supported Laminated Circular Cylindrical Roofs," *Composite Structures*, Vol. 11, No. 4, 1989, pp. 277–292.

[8]Zhou, J., and Yang, B., "A Distributed Transfer Function Method for Analysis of Cylindrical Shells," *AIAA Journal*, Vol. 33, No. 9, 1995, pp. 1698–1708.

Experimental Investigation on Blade-Stiffened Panel with Stiffener-to-Skin Fiber Stitching

Chen-Wen Chang* and Wen-Bin Young†
National Cheng-Kung University, Tainan 70101, Taiwan, Republic of China

Introduction

ADVANCED composite materials have been used in the aerospace industry because of high strength and low weight. Resin transfer molding (RTM) is believed to be one of the candidates for fabricating advanced composites with lower cost.[1,2] Application of composite materials to aircraft fuselage or wing structures offers potentially significant weight reduction relative to the metallic structures. Stiffened panels are the basic unit of these structures. Traditionally, the stiffened panels have been fabricated by the techniques of adhesive bonding or cocuring of the skin and stiffener components made of prepreg laminates. To reduce the cost, the RTM process could be used to fabricate composite stiffened panels in future aircraft.

For stiffened panel structures, improvement of the damage tolerance is still a major issue for component design. In general, a toughened resin system or three-dimensional textile fiber preform could provide some improvements. However, fiber stitching is found to be an easy and cost-effective method to enhance the properties of the composite in the thickness direction, as compared with conventional laminates. In several studies, through-the-thickness stitching of the fibrous preform was reported to improve damage tolerance and residual strength after impact of the composites.[3–5] For fuselage and wing-box structures, the stiffener-to-skin separation is one of the major considerations of the panel failure as subjected to the internal pressure, either the cabin differential pressure or the wing-box fuel tank pressure. The stiffener and skin may be stitched in an efficient way to enhance the integrity of the panel. This study investigates the reinforcing effect of stiffener-to-skin stitching on flat blade-stiffened composite panels. T-shaped composite parts, which represented a unit of the blade-stiffened panel, with fiber stitching in the joint areas were fabricated. Several types of stitching configurations were tested to evaluate the influence of stitching.

Experimental Design

The mold design consisted of three parts. The upper mold was made of a 41 × 41 × 4.6 cm 6061-T6 aluminum plate. The lower mold included two parts made of 38.1 × 20.5 × 20.2 cm T6061-T6 aluminum blocks. The inlet was located at one corner of the stiffener and two outlets at the corners of the flange. An O-ring seal was used in all of the mating parts to seal the mold and prevent leakage during the resin injection. The T-shaped structure is shown in Fig. 1.

In the RTM process, after mold filling, the mold was kept at a constant temperature for a period of time to cure the specimen. Clamping, which generated the necessary pressure during the filling and curing processes, was provided by an hydraulic press. The press also had a heat source for mold temperature control. Resin was injected into the mold using a pressure vessel connected to a compressed air source. The resin system was CIBA-GEIGY epoxy resin (Araldite LY 564 and Hardener HY 2954), and the reinforcements were made of TGFW-600 woven roving glass fiber mats with 600 g/m^2 surface density. Fiber mats were cut into the desired size and stitched using Kevlar® 49 to form the preform, then stacked into the mold by hand. The diameter of the needle was 1.3 mm,

Received Aug. 1, 1995; revision received Nov. 7, 1995; accepted for publication Dec. 5, 1995.

*Graduate Student, Institute of Aeronautics and Astronautics.
†Associate Professor, Institute of Aeronautics and Astronautics.